Colloids and Surfaces A: Physicochemical and Engineering Aspects 666 (2023) 131306

Contents lists available at ScienceDirect

Colloids and Surfaces A: Physicochemical and Engineering Aspects

journal homepage: www.elsevier.com/locate/colsurfa

Fabrication of bijels with sub-micron domains via a single-channel flow device

Alessio J. Sprockel [1], Mohd A. Khan [1], Mariska de Ruiter, Meyer T. Alting, Katherine A. Macmillan, Martin F. Haase [*]

Van't Hoff Laboratory for Physical and Colloid Chemistry, Department of Chemistry, Debye Institute of Nanomaterials Science, Utrecht University, Padualaan 8, Utrecht 3584 CH, the Netherlands

HIGHLIGHTS

- Improved control over fabrication of nanoparticle stabilized bicontinuous emulsions (bijels).
- Development of a single channel flow device for the fabrication of bijels.
- Influence of aluminum content in silica nanoparticles on bijel fabrication.
- Control of nanoparticle interfacial behavior during bijel formation.
- Printing of bijel fibers enables potential applications in liquid-liquid extraction and reactive separations.

GRAPHICAL ABSTRACT

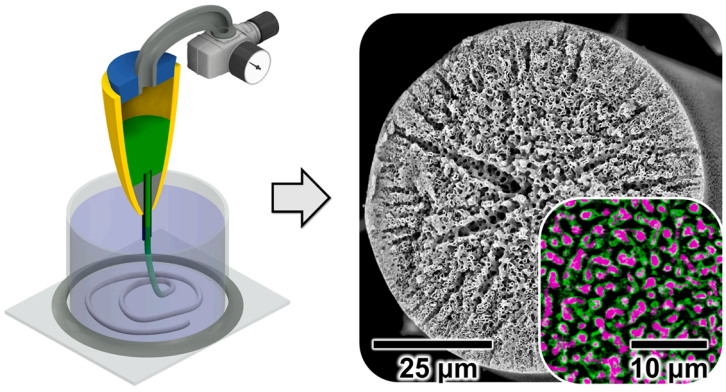

ARTICLE INFO

Keywords:
Bijels
Surfactants
Microfluidics
Nanoparticles at interfaces
Pickering emulsion
Spinodal decomposition

ABSTRACT

Particle-stabilized bicontinuous emulsions (bijels) are made of two interwoven liquid channel systems. In contrast to emulsion droplets, the liquid-liquid interface of bijels curves both towards the oil and the water phases. Thus, particles with equal wettability for both oil and water are needed to stabilize the interface. In this research paper, we enhance the understanding of nanoparticle functionalization by a surfactant for controlling the particle wettability. To this end, we develop a novel, single-channel, continuous flow method, enabling the rapid synthesis and analysis of bijels formed via solvent transfer induced phase separation (STrIPS). Silica nanoparticles are functionalized with the positively charged surfactant (cetyltrimethylammonium^{+}, CTA^{+}). Zeta-potential and colloidal stability analysis are employed to characterize the CTA^{+} functionalization. Confocal and electron microscopy are used to visualize the resulting bijel structures. Bijels with nearly uniform, sub-micrometer channels are obtained when the particle functionalization by CTA^{+} is regulated. To this end, the

Abbreviations: STrIPS, Solvent Transfer Induced Phase Separation; NP, Nanoparticles; CLSM, Confocal laser scanning microscopy; SEM, Scanning electron microscopy; TEOS, tetraethylorthosilicate; CTA+, Cetyltrimethylammonium cation; DEP, Diethylphthalate; φi, volume fraction of component i; n_i, refractive index of component i; ci, concentration of component i [mol/L]; η, interfacial attachment efficiency; Q_i, volumetric flow rate of component i [mL/h].

* Corresponding author.
E-mail address: m.f.haase@uu.nl (M.F. Haase).

[1] These authors contributed equally to this work.

https://doi.org/10.1016/j.colsurfa.2023.131306
Received 8 November 2022; Received in revised form 13 February 2023; Accepted 18 March 2023
Available online 21 March 2023

initial negative zeta-potential of the particles needs to be low enough to prevent excessive CTA^+ adsorption. The adsorption is further controlled by adjusting the concentrations of CTA^+, salt and glycerol additive. This report shows that the nanoparticle surfactant modification depends on multiple parameters, providing guidance for future bijel synthesis approaches.

1. Introduction

Bicontinuous interfacially jammed emulsion gels (bijels) are particle stabilized emulsions made of two interwoven liquids [1,2]. In a bijel, two immiscible liquids are mechanically arrested in non-equilibrium, bicontinuous arrangement via a layer of colloidal particles at the interface. This unique arrangement enables several applications of bijels. For instance, bijels have been shown to facilitate continuous flow liquid-liquid extraction [3]. Moreover, reactive separations in bijels provide opportunities for chemical process intensification [4–6]. Bijels can also be used as semipermeable separation membranes for ultrafiltration [7,8]. Furthermore, bijels have been used to template batteries with high energy densities, improved capacity retention, and enhanced mechanical stability [9–12]. Last, bijels are suitable template materials for tissue engineering with enhanced tissue integration and vascularization [13,14].

The synthesis of bijels was first proposed via computer simulations in 2005 [15]. Two years later, the first bijel was fabricated in the lab [16]. To this end, a solution of two liquids containing surface active colloids was forced to undergo spinodal phase separation by changing the temperature. During liquid-liquid demixing, the colloids attach to the interface until they form a densely packed layer. The resulting bicontinuous liquids are mechanically arrested via interfacial jamming of strongly attached colloids. Rheologically, bijels have an order of magnitude higher storage than loss modulus and glass-like nature [17,18]. Bijels can also be obtained by direct emulsification of immiscible liquids [19], yielding bijels with submicron domains when nanoparticles are combined with block copolymers [20]. A third approach to synthesize bijels is entitled solvent transfer induced phase separation (STrIPS) [21]. During STrIPS, a ternary liquid mixture containing surface active nanoparticles (NPs) generates bijels via a continuous flow process. Recently, STrIPS was further developed to prepare bijels with nearly uniform bicontinuous channels with sizes of a few hundred nanometers [3]. These nanostructured bijels show potential for applications requiring larger interfacial areas, but the fine-tuning of their structures requires simultaneous control over several parameters.

Bijels are formed via a time dependent nonequilibrium self-assembly process [22]. The complexity of this process can result in limited control and reproducibility of the bijel synthesis. In part due to this, bijels are not yet generated with a wide variety of building blocks [23–25]. To overcome the synthesis challenges, iterative bijel fabrication strategies have been introduced [26]. Moreover, to handle reproducibility problems of the bijel synthesis, machine learning tools have been used for the automation of bijel characterization [27,28]. These developments highlight the need for rapid screening tests to gain control over bijel synthesis.

What makes bijel synthesis experimentally challenging is the strict requirement for the particle surface chemistry [29]. In contrast to particle stabilized emulsion droplets [30–32], the stabilization of bijels requires precise control over the particle amphiphilicity [29]. For example, to generate bijels with silica particles, their surfaces need to provide equal wettability for both immiscible liquids. But, bare silica particles are not suitable to stabilize the bijel due to their hydrophilic, negatively charged surfaces. Thus, bijel stabilization demands a surface functionalization of the silica particles. *In-situ* surface functionalizations with surfactants enable the direct use of bare silica particles for bijel stabilization [33–37]. The desired neutral wettability can be obtained by controlling the amount of adsorbed surfactant. However, the *in-situ* surface functionalization depends on a multitude of parameters, for example pH value, chemical composition of the particles, surfactant concentration, and salt concentration. This complexity demands experimental techniques that allow for the testing of many samples in a short time. The resulting control can facilitate the synthesis of bijels with maximized interfacial areas and nearly uniform bicontinuous domains for target applications such as reactive separations [4–6], membranes [7,8], batteries [9–12] and tissue engineering [13].

Here, we introduce a simplified bijel synthesis method via solvent transfer induced phase separation (STrIPS) that allows for fast bijel sample preparation. Combined with confocal laser scanning microscopy (CLSM), this technique enables the rapid assessment of the bijel structure. Before making bijels, we investigate the stability of the bijel precursor mixture in detail. After that, we demonstrate how the fast sample preparation technique facilitates the systematic investigation of the bijel structure in dependence of various parameters. Here, these parameters include the surface chemistry of the particles, surfactant concentration, pH value, and the effects of additives. Last, we show how the knowledge gained from the rapid screening technique allows for the printing and alignment of bijel fibers with well-defined structures and controllable diameters.

2. Materials and methods

2.1. Materials

All chemicals were used as received. Hexadecyl-trimethylammonium bromide (CTA^+, >99%), 1-propanol (>99.5%), Nile red (for microscopy), tetraethyl orthosilicate (TEOS, >99%), sodium hydroxide (≥99%), sodium chloride (≥99%) and mineral oil were purchased from Sigma-Aldrich. The silica nanoparticles (Ludox TMA) were kindly provided by Grace GmbH with batch number – 1000374513 (Batch-1) and Lot number-2021850133 (Batch-2). Diethyl phthalate (DEP, 99%), toluene (99.85%), n-hexane (99% HPLC), glycerol (>99%), hydrochloric acid (HCl, 37% pure) were received from Acros organics.

2.2. Assembly of bijel fiber extrusion device

A detailed description of the device can be found in SI Section 2. In brief, a 5 cm long borosilicate glass capillary (50 μm inner diameter, 80 μm outer diameter, VitroCom CV0508) is placed in a disposable 200 μL or 1 mL plastic pipette tip. A few microliters of Norland adhesive 81 is added into the tapered end of the pipette tip, with the front of the glass capillary sticking out by ~ 5 mm. The assembly is irradiated with a handheld UV-lamp (365 nm) for 1 min. Afterwards, the overhanging longer part of the capillary sticking out from the back of the pipette tip is broken off at the base of the solidified glue.

2.3. Preparation of Ludox TMA particles and fiber precursor mixture

2.3.1. Ludox TMA particle dispersion

The precursor mixtures are made with well-defined Ludox TMA dispersions. The dispersions can be prepared via (i) a slow or (ii) a fast method. Throughout the manuscript, the slow method has been used. However, we recommend the use of the fast method for future rapid screening tests. (i) The slow method involves the concentration of the Ludox TMA dispersion (typically 100 mL) from 34 wt% to 40 wt% in a rotary evaporator at 60 °C and 140 mbar. First, the pH value of the dispersion is adjusted to 3 by adding a few hundred μL of 1 M HCl followed by increasing the particle concentration. After this, the dispersion

is centrifuged at 3500 rpm for 10 min to remove any aggregates formed, followed by re-adjusting the pH to 3 by adding 1 M HCl. Next, the dispersion is transferred into a dialysis bag (Spectra/Por MWCO 14000) and placed into a 2 liter beaker filled with water at a specific pH value (variable for Fig. 4, otherwise pH 3) and specific NaCl concentrations (variable for Fig. 7, otherwise 21.6 mM in the precursor mixture). (ii) For the fast method, the pH value and salt concentration of the Ludox TMA dispersions from the supplier are directly adjusted. To this end, 1 M HCl and NaCl crystals are added directly (see SI Section 5). The particles are concentrated in the rotary evaporator to 40 wt%. However, also this concentration step can be avoided, because the concentration provided by the manufacturer (34 wt%) is sufficient for the stabilization of the bijel. The Ludox TMA dispersions obtained via the fast or the slow method are mixed with the other components of the precursor mixture as described next.

2.3.2. Bijel precursor mixture

A solution of 200 mM CTA^+ in 1-propanol, and a solution of 50 wt% glycerol in 1-propanol are separately prepared. Calculated volumes of the Ludox TMA dispersion ($V_{TMA,H2O}$, containing 40 wt% Ludox TMA), pure 1-propanol ($V_{1\text{-prop}}$), the solutions of CTA^+ ($V_{CTA+,1prop}$) and glycerol ($V_{Glyc,1prop}$) in 1-propanol, and DEP (V_{DEP}) are combined to obtain the precursor mixture with the volume fractions $\varphi_{DEP} = 0.079$, $\varphi_{water} = 0.432$ (pure water, excluding the volume of the silica particles), $\varphi_{Glycerol} = 0.106$, and $\varphi_{1\text{-propanol}} = 0.383$. To agree with the phase diagram in Fig. 1A, all volume fractions listed here are based on the liquids alone and exclude the volume of the particles. The CTA^+ and NaCl concentrations specified in the main text take the volumetric sum of the 4 liquids (water, glycerol, 1-propanol, DEP) as the basis. Additionally, the basis for the particle mass fraction is the sum of the masses of the 4 liquids plus the mass of the particles. For example, to prepare a precursor mixture of a total volume 3 mL with 23 wt% Ludox TMA particles, 29.2 mM CTA^+, 21.6 mM NaCl, $\varphi_{Glycerol} = 0.106$ the following volumes are mixed: $V_{TMA,H2O} = 1.500$ mL, $V_{1\text{-prop}} = 0.448$ mL, $V_{CTA+,1prop} = 0.387$ mL, $V_{Glyc,1prop} = 0.455$ mL, $V_{DEP} = 0.210$ mL. Additional details about the method for preparing fiber precursor mixtures and bijel fibers can be found in reference [3].

2.4. Visualization of fiber flow

A Nikon LV100 microscope is rotated by 90 degrees to obtain a horizontal orientation of the objective. The microscope focuses with a 20x objective on the capillary orifice of the extrusion device depicted in Fig. 2B. Air pressure is applied to control the precursor mixture flow rate. The fiber flow is recorded with a Photron Nova highspeed camera attached to the microscope.

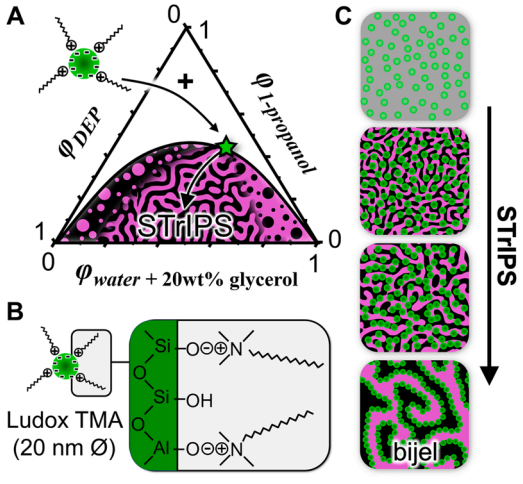

Fig. 1. Basics of bijel synthesis via STrIPS. A Phase diagram of diethylphthalate, water, glycerol and 1-propanol. Compositions on the axes are given as volume fractions (φ_i). B Schematic depiction of Ludox TMA nanoparticle interaction with cetyltrimethylammonium cations (CTA^+). C Schematics of bijel formation by spinodal phase separation and interfacial jamming of CTA^+ modified Ludox TMA nanoparticles.

2.5. Zeta-potential measurements

Particles are concentrated and dialyzed via the slow method described in 2.3, Preparation of fiber precursor mixture. For each acidity and TMA batch in Fig. 4B a separate dialysis is performed. 3 droplets of the dialyzed particle dispersion (40–45 wt%) are diluted with 4 mL of the corresponding dialysis water (of equal pH and NaCl concentration). For each sample the zeta potential is measured three times on a Malvern Zetasizer Ultra using DTS1070 cuvettes. The sample is allowed to equilibrate at 25 °C for 120 s before each measurement.

2.6. Confocal microscopy analysis

The toluene surrounding the fibers made with the extrusion device in the sample container is replaced with hexane via 3–4 subsequent washing steps. Last, hexane, saturated with Nile red is added. The sample container is closed with a lid and transferred to the stage of a Leica Stellaris 5 inverted confocal laser scanning microscope. Two separate excitation lasers (488 nm and 561 nm) are used to excite the Nile red in hexane, and the adsorbed Nile Red. Confocal micrographs are acquired with fluorescence emission detection ranges 500–530 nm and 600–700 nm. The spectra in Fig. 3C are obtained with the spectral analysis plugin of the Leica LASX software.

2.7. Scanning electron microscopy analysis

In order to prepare samples for scanning electron microscopy, the bijel fibers are placed into 3 wt% TEOS in mineral oil. After a duration of 24 h, the fibers were washed with hexane and dried at room temperature. The samples are sputter-coated with platinum (8 nm thickness) before imaging with a Zeiss EVO Scanning Electron Microscope operated at 15 kV.

2.8. X-ray fluorescence analysis

To determine the elemental composition of the two Ludox TMA batches, X-ray fluorescence spectroscopy (XRF) was performed on these particles. 10 mL of the bare dispersions were dried for 24 h at 200 °C to obtain a dried powder composed of particles. 600 mg of each batch were mixed with lithium borate, molten and casted into a pearl mold. The analysis were performed in Uniquant mode on a XRF Thermo Scientific ARL Peform'X.

3. Results and discussion

3.1. Rapid method for bijel synthesis

Solvent transfer induced phase separation (STrIPS) generates bijel fibers via liquid-liquid phase separation of a multicomponent precursor mixture. The mixture is composed of the 4 liquids: water, glycerol, 1-propanol, and diethyl phthalate (DEP). The mixture further contains Ludox TMA nanoparticles (NPs) and a surfactant (cetyltrimetylammonium bromide; CTA^+). Water and glycerol are fully miscible. In contrast, DEP does not mix with water, nor with glycerol. However, DEP, water, and glycerol all mix with 1-propanol. Thus, 1-propanol enables the preparation of a homogeneous solution of all 4 liquids. We determine the volumes of 1-propanol required to mix DEP with water and glycerol via turbidimetry (see SI Section 1). This analysis yields the binodal curve in the triangular phase diagram shown in Fig. 1A. In this diagram, the horizontal axis depicts the volume fraction

of a solution of 20 wt% glycerol in water, while the diagonal axes give the volume fractions of 1-propanol and DEP. Mixing compositions above the binodal curve results in transparent solutions. The composition of these solutions falls below the binodal curve during STrIPS due to the removal of 1-propanol [38].

STrIPS is realized with miscible liquid compositions above the critical point (shown as a green star in Fig. 1A). The critical point is determined by confocal microscopy analysis (see SI Section 1). Based on the critical point, the liquid volume fractions (φ_i) in the precursor mixture are selected to be: $\varphi_{DEP} = 0.079$, $\varphi_{water} = 0.432$, $\varphi_{Glycerol} = 0.106$, and $\varphi_{1\text{-propanol}} = 0.383$. A typical mixture additionally includes 23 wt% Ludox TMA NPs, 29.2 mM CTA^+ and 21.6 mM NaCl.

The Ludox TMA NPs can be homogeneously dispersed in the precursor mixture due to their interaction with CTA^+. CTA^+ molecules adsorb electrostatically on anionic silanol (SiO^-) and aluminate (AlO^-) groups on the NPs (Fig. 1B). The CTA^+ modification also makes the NPs surface active by changing their wettability for the oil and water. Fig. 1C schematically depicts bijel formation via STrIPS. STrIPS initializes spinodal phase separation, resulting in bicontinuous DEP/water channels that coarsen over time. The NPs arrest the bicontinuous DEP/water structure via interfacial jamming, if the CTA^+ modification enables equal wettability for both DEP and water on the NPs. In the following, we introduce a fast and reproducible technique to test the outcome of the process depicted in Fig. 1C, enabling the rapid determination of the conditions to achieve equal wettability for the particles.

Bijel fibers with reproducible structures can be obtained with a simple injection technique of the precursor mixture into toluene. This approach enables the rapid preparation of tens of different bijel fiber samples per day. Such rapid screening enables the testing of new compositions, NP types, and surfactants. Previously, microfluidics with co-axial capillaries has been used for the synthesis of bijel fibers with diameters of 50–100 μm. Maintaining the fiber diameter below 100 μm is important for controlling the diffusion limited STrIPS process. However, the assembly of the microfluidic devices and their operation are time-consuming. As an alternative to co-axial microfluidics, we demonstrate that bijel fibers with diameters below 100 μm can also be obtained with a single capillary: A 50 micrometer inner diameter glass capillary with a length of ~ 1 cm is glued into a disposable plastic pipette tip (see SI Section 2). For each precursor mixture to be tested, one of these assemblies is crafted. Around 50 microliters of the precursor mixture is filled into the space above the inlet of the glass capillary in the pipette tip. The outlet of the glass capillary is submerged into 2 mL of toluene, contained within a cylindrical glass vial that has been glued onto a microscope cover slip. Laboratory tubing is connected to the pipette tip via an adapter. The air pressure above the precursor mixture is controlled via a regulator. By increasing the air pressure above atmospheric pressure, the precursor mixture flows out continuously as a fiber from the capillary into toluene as depicted in Fig. 2A.

The diffusion of 1-propanol into toluene triggers phase separation during the flow of the precursor mixture out of the capillary. It is likely, that also toluene diffuses into the fiber to gradually replace the DEP during STrIPS. At the same time, the Ludox TMA NPs deposit onto the interface between the two phases. The particle deposition rigidifies the phase separated material, preserving the cylindrical shape of the fiber. The rigidification takes place due to the surface functionalization of the NPs with CTA^+. Bare Ludox TMA NPs are hydrophilic and prefer to reside in the water phase. The adsorption of CTA^+ onto the NPs renders them interfacially active by increasing the NP hydrophobicity. Once the NPs form a sufficiently dense interfacial layer, they jam the interface and mechanically arrest the microscopic arrangement of the two liquid phases as depicted in Fig. 1C.

Fig. 2B shows brightfield microscope images of the precursor mixture flowing out as a viscoelastic fiber from the capillary. The downward movement of the solidified fiber surface drags the toluene along, schematically depicted by velocity arrows. The diameter of the fiber can be controlled with the pressure of the precursor mixture as plotted in Fig. 2C. The fiber likely flows out at 0 bar pressure gauge reading due to a combination of gravity and residual pressure in the tubing. Higher pressures increase the flow rate of the precursor mixture, resulting in thicker fibers. The fiber sinks to the bottom of the glass cylinder due to the higher density of the precursor mixture. It lands on the microscope cover-slip, where it builds up over time. The design of the sample container enables immediate inspection of the fiber via bright field microscopy.

3.2. Microscopy of bijel fibers

Optical microscopy allows for the assessment of the bijel fiber transparency. To this end, the sample container is placed on an inverted microscope stage as depicted on the right of Fig. 2A. In the following, we show that enhancing the optical transparency of the fibers facilitates a detailed characterization of the internal structure via confocal laser scanning microscopy (CLSM). The micrographs in Fig. 3A-i show that the fibers appear opaque in toluene, indicating that their internal structure scatters light. In contrast, the micrographs in Fig. 3A-ii show that the fibers become partially transparent after exchanging toluene with hexane. The magnified inset of the fibers in hexane reveals regions of different contrast, indicating a porous interior. The enhanced transparency of the fibers can be explained by the improved refractive index matching with hexane as compared to toluene. The refractive index of

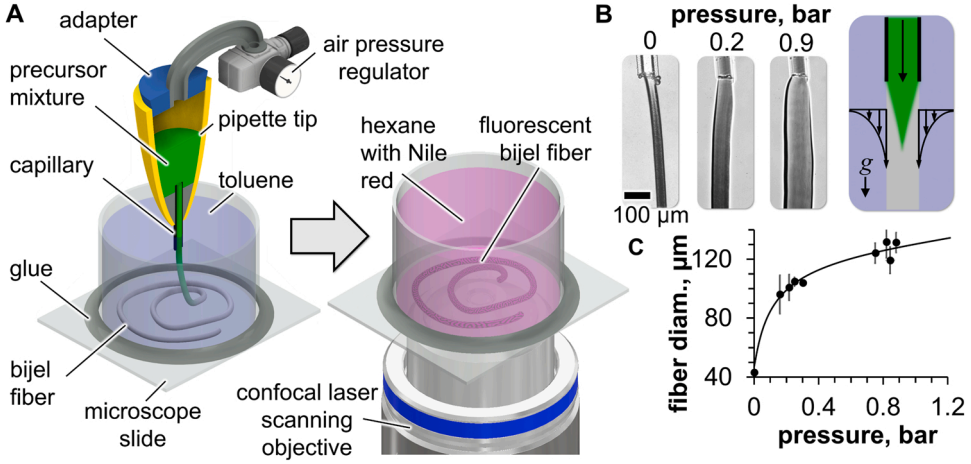

Fig. 2. Basics of bijel fiber sample preparation. A Experimental setup to prepare bijel fiber samples for laser scanning confocal microscopy analysis (Partial cutaway). B Bright field microscope images of pressure driven outflow of the precursor mixture into toluene. C Fiber diameter dependence on precursor mixture pressure.

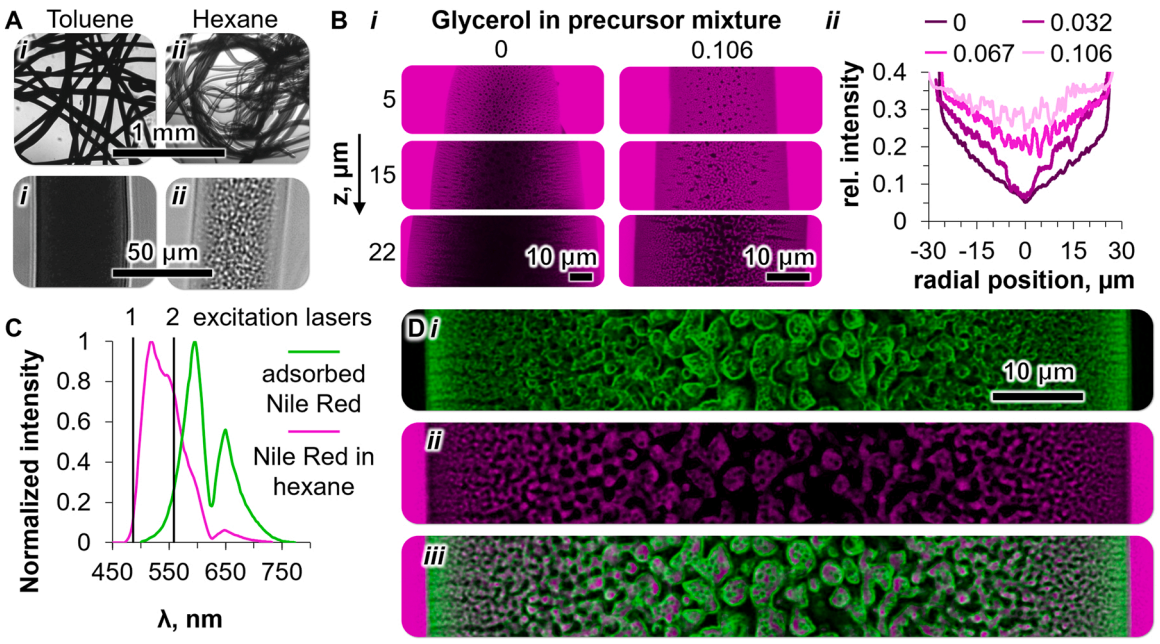

Fig. 3. Brightfield and confocal laser scanning microscopy (CLSM) characterization of fibers. A Bright field microscope image of fibers in *i.* toluene and *ii.* hexane. B *i.* CLSM images of oil channels at different confocal planes (z-stack) of fibers made with different glycerol volume fractions ($\varphi_{Glycerol}$) in the precursor mixture. *ii.* Relative fluorescence intensity (normalized by the fluorescence signal outside of the fibers) against the radial position of the fiber for different glycerol volume fractions ($\varphi_{Glycerol}$) C Fluorescence spectra of Nile red in hexane (magenta) and adsorbed to the NPs (green), both spectra are normalized with their respective maximum peaks. D Cross-sectional CLSM image of a fiber with fluorescence signal of Nile red *i.* adsorbed on particles (green) and *ii.* dissolved in hexane (magenta). The fiber was synthesized with 29.2 mM CTA^{+}, $\varphi_{Glycerol} = 0.106$, and 21.6 mM NaCl in the precursor mixture. iii. Shows the overlay of both channels.

toluene is $n_{toluene} = 1.496$ and that of hexane is $n_{hexane} = 1.379$. The major volumetric fraction in the fiber consists of water with $n_{H2O} = 1.333$, while glycerol ($n_{glycerol} = 1.472$) and silica particles ($n_{silica} = 1.459$) make up smaller volume fractions. After the toluene in the container is exchanged by hexane, the hexane diffuses into the fiber. The reduced value of n_{hexane} compared to $n_{toluene}$ results in less light scattering by the porous interior of the fiber, because the refractive index contrast to the water phase decreases. For CLSM characterization, the fiber transparency is further enhanced, as discussed next.

CLSM reveals the spatial distribution of hexane within the fibers. Hexane with dissolved Nile Red is added to the sample container holding the fibers. In the CLSM, a blue laser (488 nm) is employed to excite the fluorescence of Nile Red in hexane (shown in magenta color in Fig. 3B-i). Near the surface of the fiber, the maximum fluorescence intensity is observed. As the confocal plane is moved deeper into the fiber, the intensity of the fluorescence signal decreases. The intensity decrease results from light scattering due to imperfect refractive index matching. We can enhance the refractive index match by increasing the amount of glycerol added to the precursor mixture. Glycerol partitions to water, increases n_{H2O} and reduces the mismatch with n_{hexane}. The CLSM images in Fig. 3B-i show that with $\varphi_{Glycerol} = 0.106$ a brighter fluorescence signal deeper within the fibers is detected. The relative fluorescence intensity is plotted over the fiber radius for different glycerol contents in Fig. 3B-ii. The radial profiles show that the relative fluorescence intensity decreases less over the radial fiber coordinate when the glycerol content is increased. The enhanced transparency enables the detailed structure analysis via CLSM in the center of the fibers as discussed in the following.

Nile Red not only fluorescently labels hexane in and around the fibers, but also the NPs within the fiber. The labeling of the NPs is possible because Nile Red adsorbs on the NP surfaces. Nile Red likely co-adsorbs on the NP scaffold due to cooperative interactions with the already adsorbed CTA^{+}. We conclude this because in the absence of CTA^{+}, Nile Red does not fluorescently label the NPs. Interestingly, this adsorption also changes the fluorescence emission color of Nile Red, as can be seen in the fluorescence spectra of Fig. 3C. The emission in the range of 630–700 nm of a fiber cross-section is visible in the CLSM image of Fig. 3D. The CLSM image reveals the contorted scaffold of NPs in the fiber. The fluorescence color change possibly results from the solvatochromic properties of Nile Red [39]. Combining the fluorescence signal of the adsorbed Nile Red with the Nile Red fluorescence in hexane from Fig. 3D-ii gives the CLSM image in Fig. 3D-iii.

The structure in Fig. 3D-iii provides an example of a variety of different architectures within the fiber. An interwoven network of hexane and water channels with NPs at the interface is found. The channel sizes increase from the fiber surface inward. The bicontinuous arrangement of water and hexane does not change over the course of 3 days, as observed by confocal microscopy. The structure primarily depends on the composition of the precursor mixture. In the following, we investigate the effects of CTA^{+}, glycerol, and NaCl concentrations on the fiber structures to understand the mechanisms behind phase separation and interfacial jamming. We begin our discussion by investigating the colloidal and phase stability of the fiber precursor mixture.

3.3. Fiber precursor mixture stability analysis

Fig. 4A-i shows photographs of the precursor mixture at three distinct physical states: 1. phase separated, 2. stable, and 3. aggregated. Which one of these three states is observed depends on the CTA^{+} concentration (c_{CTA+}) and the pH value of the aqueous NP dispersion. For the following discussion, all samples have been prepared at a fixed liquid composition ($\varphi_{DEP} = 0.079$, $\varphi_{water} = 0.432$, $\varphi_{Glycerol} = 0.106$, and $\varphi_{1\text{-}propanol} = 0.383$), NP weight fraction (23 wt%), and NaCl concentration (21.6 mM). Fig. 4A-ii provides an overview of the physical states of the precursor mixtures in dependence of c_{CTA+} and pH values.

The top row at pH = 3.25 (red dashed region) shows a remarkable trend with increasing c_{CTA+}. At $c_{CTA+} = 5$ mM, two distinct liquid phases are observed. The water rich phase is heavier and forms the bottom layer. The slight turbidity of the lower phase indicates that the NPs have partitioned into water. Also for $c_{CTA+} = 10$ mM a biphasic mixture is

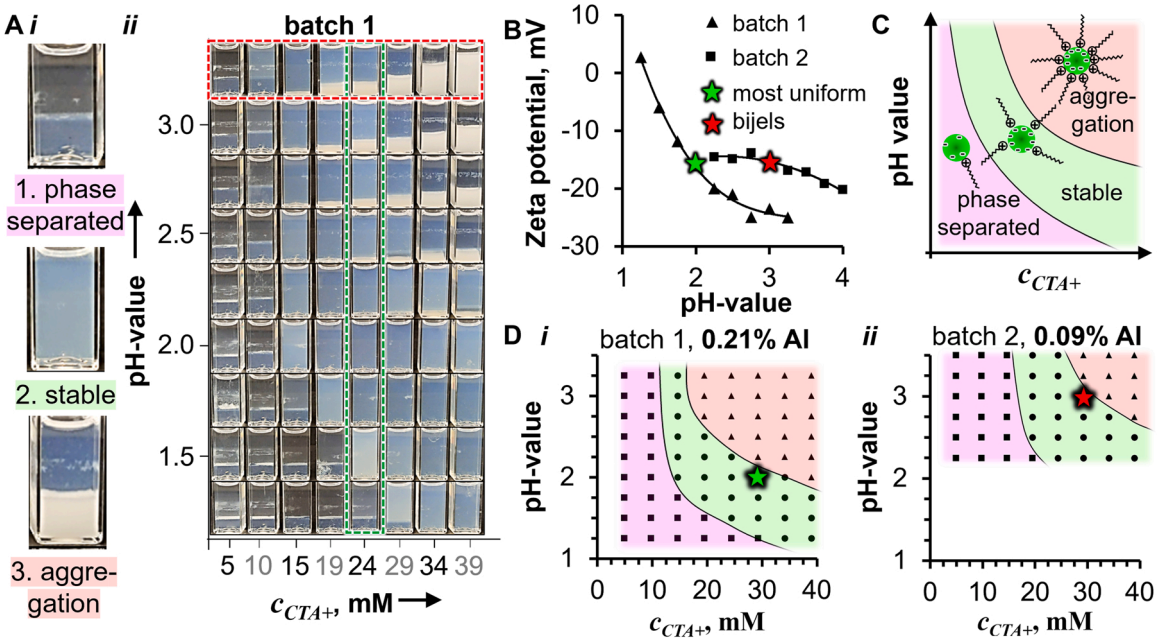

Fig. 4. Precursor mixture stability and Ludox TMA batch variability. A Photographs of fiber precursor mixtures prepared with batch 1 at different pH-values and CTA^+ concentrations (c_{CTA+}), B Zeta-potential measurements of two different batches of Ludox TMA NPs. The batch to batch variation is further shown in SI Section 7–9. C State-diagram for batch 1 with schematic depiction of CTA^+ modified NPs. D State-diagrams of the fiber precursor mixture for the two different Ludox TMA NP batches.

observed, but here top and bottom phases are turbid. The turbidity in both layers suggests that the particles distribute between the water and DEP rich phases. Interestingly, at $c_{CTA+} = 15$ mM, the phase boundary disappears and a single, liquid phase is observed. In contrast, without NPs, the precursor mixture remains homogeneous for all CTA^+ concentrations. The transition from immiscible to miscible in the presence of NPs shows that the position of the binodal curve in Fig. 1A depends on c_{CTA+}. Miscibility of the two phases can be achieved by adding more propanol, but this would change the composition away from the critical point (Fig. 1A), compromising bijel formation via spinodal decomposition. As c_{CTA+} is further raised from 15 to 19 mM, a white sediment forms. The sediment height grows and the turbidity in the supernatant decreases with increasing c_{CTA+}. This observation demonstrates that the NPs aggregate at high c_{CTA+}.

An analogous trend can be observed in a vertical column at constant $c_{CTA+} = 24$ mM (green dashed region) by increasing the pH. For pH ≤ 1.25 two distinct phases are present. Increasing to pH = 1.5 results in a single liquid phase with homogeneously dispersed NPs. At pH = 2.75 the white sediment of aggregated NPs appears, growing in height as the pH is further increased.

That the variation of two independent parameters results in the same physical phenomena suggests that both control the same property of the system: The adsorption of CTA^+ on the NPs. By raising c_{CTA+}, the adsorbed amount of CTA^+ on the NPs increases. Also by raising the pH, more CTA^+ adsorbs. The pH increase causes the silanol groups on the NPs to become more negatively charged due to deprotonation. Zeta-potential measurements of the NPs in water confirm the increasing negative charge with a raise in pH (Fig. 4B, batch 1). More negatively charged silanol groups result in additional adsorption sites for CTA^+. Thus, we can interpret our findings: At low pH and c_{CTA+}, only small amounts of CTA^+ adsorb on the NPs. For this state, the polar silanol and aluminate surface groups render the particles hydrophilic, triggering phase separation and partitioning of particles to water. At intermediate pH and c_{CTA+}, the CTA^+ adsorption increases to an optimum compatibility with the liquid mixture. This results in a single liquid phase with dispersed particles having zeta-potentials in the range from −8 to −4 mV (SI Section 8). At high pH and c_{CTA+}, excessive CTA^+ adsorption renders the particles hydrophobic, resulting in aggregation. We summarize our interpretation graphically in the state-diagram of Fig. 4C.

The position and size of the regions in the state-diagram depend on the batch of the commercial grade Ludox TMA NPs. Fig. 4D compares the state-diagrams for batch 1 and 2. For batch 2, the phase separated and stable regions are larger in the pH range 2–3.5, while the aggregated region is smaller. According to the discussion in the previous paragraph, this implies that for batch 2 less CTA^+ adsorbs on the particles for a given c_{CTA+} and pH.

Our investigation suggests that the two batches differ in their interaction with CTA^+ because of different amounts of aluminate surface groups (Fig. 1B). Combined analysis of Ludox TMA via x-ray fluorescence (XRF) spectroscopy with inductively coupled plasma optical emission spectrometry (ICP-OES) shows that batch 1 contains 0.21% aluminum and batch 2: 0.09% aluminum (see SI section 9). The XRF/ICP-OES measurements suggests that the particles of batch 1 have more negatively charged $Al\text{-}O^-$ groups on their surfaces. To test this hypothesis, we compare the zeta-potentials at variable pH values for both batches. Fig. 4B shows that above pH 2, batch 1 has a more negative zeta-potential compared to batch 2, supporting our hypothesis. Compared to silanol groups, the aluminate groups are more negatively charged at acidic pH values [40–42]. Higher aluminate contents result in more negative charge of the nanoparticles and broader pH ranges for colloidal stability [43]. Thus, batch 1 interacts more strongly with CTA^+ at a given pH, changing the stability regions of the state-diagrams in Fig. 4D.

We end this section by noting that Fig. 4 provides information about the colloidal- and phase stability of only two different Ludox TMA batches. However, future batch-to-batch variations of the commercial grade Ludox TMA NPs can change these state-diagrams. For most applications, the small variation in aluminum content is likely not important, but in achieving *in-situ* equal wett ability via CTA^+ adsorption it has proven to be of impact.

3.4. Structure dependence on CTA^+ concentration

Based on the state-diagram, stable precursor mixtures are selected

for the fiber synthesis with the experimental setup in Fig. 2A. The fibers are submerged in hexane containing Nile Red for refractive index matching and fluorescent labeling. Fig. 5A shows CLSM images of fibers made with different c_{CTA+}. An optimum value for c_{CTA+} gives the most uniform bijel structures. At the lowest c_{CTA+} = 19.4 mM, the fiber contains an unorganized fluorescence signal from the adsorbed Nile red on the particles (shown in green). No well-defined structures can be obtained here. In contrast, for c_{CTA+} = 29.2 mM, a well-defined network of interwoven water and hexane channels with widths of 300 – 800 nm is observed.

For c_{CTA+} = 29.2 mM, the NPs form a distinct green layer at the interface of the channels. We define this as the most uniform bijel structure. Interestingly, previous research has shown that an emulsion inversion from oil-in-water to water-in-oil takes place close to c_{CTA} = 29 mM (see SI Note 14 in [3]). The emulsion inversion suggests that the CTA^+ modified Ludox TMA particles are equally wetted by oil and water near c_{CTA} = 29 mM.

For both Ludox TMA batches, the most uniform bijel structure is found at c_{CTA+} = 29.2 mM. However, to obtain this structure, the pH value of the aqueous NP dispersion must be pH = 2 for batch 1, and pH = 3 for batch 2. Interestingly, at these two pH values the zeta-potentials of both NP batches in water are at −16 mV, suggesting that their surface charge densities are similar. We highlight the parameter combination for the most uniform bijel structures for batch 1 with a green and batch 2 with a red star in Fig. 4B and D.

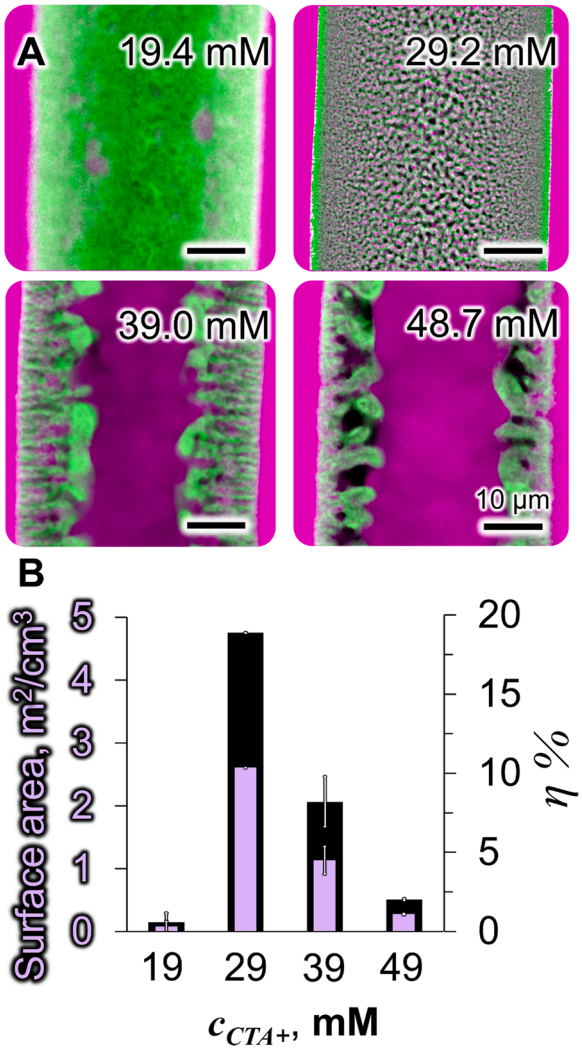

Fig. 5. CLSM analysis of fiber structures. A CLSM micrographs of the fiber equator at different c_{CTA+} (batch 2, $\varphi_{Glycerol}$ = 0.106, 21.6 mM NaCl, for c_{CTA+} = 19.4 mM and 29.2 mM a pH value of 3 was used, for c_{CTA+} = 39.0 mM and 48.7 mM a pH value of 2.5 was used to enable colloidal stability). B Surface area and interfacial NP attachment efficiency (η) in dependence of c_{CTA+}. Scale bar is 10 μm for all images.

Above the optimum c_{CTA+} = 29.2 mM, the uniformity of the fiber structures decreases. To prepare colloidally stable samples at higher c_{CTA+}, the pH value of the aqueous fraction was lowered to 2.5. c_{CTA+} = 39 mM results in the appearance of radially aligned channels near the outer surface of the fiber and a central hexane filled cavity. Further increasing c_{CTA+} to 48.7 mM and above yields a hexane filled hollow fiber with coarse radial channels. Notably, at c_{CTA+} = 48.7 mM water (black) appears to have separated from the particles, possibly indicating the dewetting from the particle surfaces.

From the CLSM images obtained with different c_{CTA+}, the interfacial area between hexane and water can be measured via image analysis (see SI Section 3). We normalize the interfacial area with the fiber volume and find a maximum of 2.6 m^2/cm^3 for the most uniform bijels at c_{CTA+} = 29.2 mM. With this area, the amount of NPs on the interface can be estimated. For this calculation, we assume that the NPs form a hexagonally packed monolayer on the interface and that each particle occupies an area equivalent to its own cross-section. We define the NP attachment efficiency (η) as the ratio of particles at the interface to particles added to the initial precursor mixture (see SI Section 3 for details of the calculation). For c_{CTA+} = 29.2 mM, η reaches a maximum of 19%, while for the highest and lowest c_{CTA+}, η drops below 2.5%. The relatively low values for η raises the question whether STrIPS bijels can also be stabilized with lower particle weight fractions than reported here, a question to be answered in future research.

3.5. Structure dependence on glycerol content

η also depends on the glycerol content in the precursor mixture. Fig. 6A provides an overview of magnified CLSM images of fibers synthesized with precursor mixtures of different c_{CTA+} and $\varphi_{Glycerol}$. Despite the loss of fiber transparency at low glycerol contents, high laser intensities enable visualization of the fiber center by CLSM. The channel network becomes more uniform when going from the upper right to the lower left corner in the overview. At c_{CTA+} = 31.6 mM and $\varphi_{Glycerol}$ = 0, the hexane channels are clogged with aggregated NPs. In contrast, for c_{CTA+} = 24.3 mM and $\varphi_{Glycerol}$ = 0.106 the NPs form a distinct layer at the hexane/water interface. There are also spherical water inclusions in the pink hexane with NPs on their interfaces. From the CLSM images, we measure the interfacial area, calculate η and plot the results in the bar diagram of Fig. 6B. At $\varphi_{Glycerol}$ = 0.106 (red dashed box and curve in Fig. 6A&B), an increase of c_{CTA+} causes the hexane channels to become smaller (Fig. 5A). This results in an increase of η from 10.0% to 14.3% (Fig. 6B). In contrast, at $\varphi_{Glycerol}$ = 0, the same increase of c_{CTA+} causes the hexane channels to become bigger, resulting in a decrease of η from 11.2% to 7.0% (blue dashed box and curve in Fig. 6A&B). The trends show that with added glycerol less coarsening takes please before the NPs stabilize the bicontinuous channel network during STrIPS. The precise mechanism for how glycerol influences bijel formation is unknown. It is unlikely that glycerol increases the viscosity of the water phase, since viscosity measurements show that for the values of $\varphi_{Glycerol}$ employed here, the viscosity is close to that of pure water [44]. More research is needed to understand the role of glycerol during bijel formation.

3.6. Structure dependence on NaCl concentration

We have seen that the CTA^+ functionalization of the NPs depends on the pH value, c_{CTA+} and the $\varphi_{Glycerol}$ in the precursor mixture. The last physicochemical parameter investigated here is the sodium chloride concentration in the precursor mixture (c_{NaCl}). We employ scanning electron microscopy (SEM) to analyze the fiber structures, because some of the samples do not contain bicontinuous channel networks, limiting

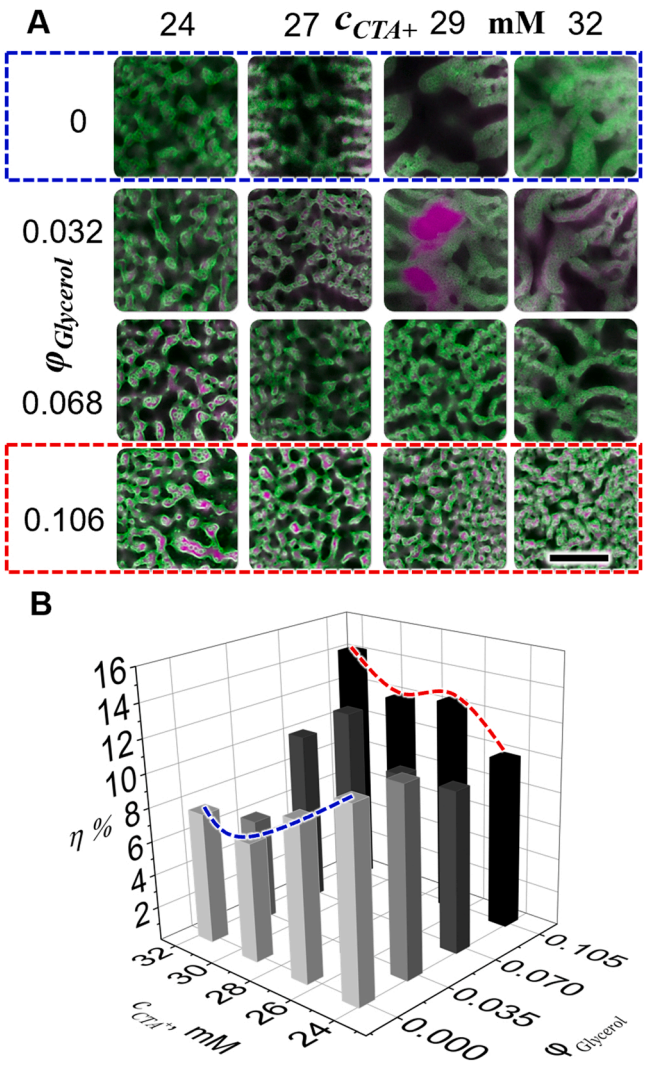

Fig. 6. Combined c_{CTA+} and $\varphi_{Glycerol}$ effect. A CLSM images of the fiber centers prepared with different c_{CTA+} and glycerol contents. B Interfacial attachment efficiency η in dependence of c_{CTA+} and glycerol volume fraction $\varphi_{Glycerol}$. Scale bar is 10 μm for all images.

the visualization via CLSM since Nile red cannot readily diffuse into the structure. Since the SEM analysis takes place in vacuum, the fibers must be dried. However, drying of the fibers causes the NP scaffold to collapse due to capillary stresses during evaporation and the removal of the toluene/water interfaces (see SI Section 4). To avoid collapse, the NP scaffold is reinforced with tetraethyl orthosilicate (TEOS). After fiber synthesis, toluene around the fibers is exchanged with a solution of 3 wt % TEOS. The fibers are left in this solution for 24 h.

Afterwards, the TEOS solution is removed via multiple washes of hexane and the fibers are air dried. Fig. 7 provides an overview of SEM images of fibers prepared with variable c_{CTA+} and c_{NaCl}.

The SEM images show that a minimum c_{NaCl} is needed to generate bicontinuous channels within the fiber. To control c_{NaCl}, the aqueous NP dispersion is dialyzed in water at different c_{NaCl} and a constant pH value of 3. Alternatively, adding NaCl directly to the commercially available Ludox TMA dispersion yields similar trends (see SI Section 5). The red dashed region at c_{CTA+} = 29.2 mM in Fig. 7 shows that for c_{NaCl} ≤ 4.3 mM, the fibers are filled with microscopic spheres. The sphere sizes increase from ≈ 500 nm to 1 μm when c_{NaCl} is increased from 0 to 4.3 mM. For $c_{NaCl} \geq$ 17.2 mM, the structure transitions to a bicontinuous channel network. The sizes of the oil filled channels in the fiber center decrease from ≈ 1 μm to ≈ 300 nm as c_{NaCl} is increased from 21.6 to 25.9 mM. The NaCl variation shows that c_{NaCl} influences the NP modification by CTA^+ and that a minimum c_{NaCl} = 17.2 mM is needed to enable the formation of bicontinuous structures in the fibers. Fig. 7 shows a similar trend as was observed in Fig. 5A when increasing c_{CTA+}. The green dashed region demonstrates that raising c_{CTA+} from 19.5 to 48.7 mM at c_{NaCl} = 21.6 mM results in a drastic transition of the fiber structure. At c_{CTA+} = 19.5 mM a poorly NP stabilized interior is formed. In contrast, for 24.3 mM ≤ cCTA+ ≤ 29.2 mM nearly uniform bicontinuous channel networks are obtained.

Raising c_{CTA+} to 48.7 mM results in a hollow fiber with anisotropic radial channels. For Fig. 7, the fibers have been fabricated with a Ludox TMA batch of a wider stability region in the state diagram as compared to batch 2. Thus, the utilization of higher c_{CTA+} in the precursor mixture was possible without particle aggregation.

3.7. Control of bijel fiber production rate, diameter and alignment with microfluidics

Within the first part of this paper, the influence of pH value, Ludox TMA batch, c_{CTA+}, $\varphi_{Glycerol}$, and c_{NaCl} on the structures of the fibers was tested. It was found that a variety of different fiber morphologies can be obtained. Rapid screening of the parameters and their interdependencies were realized via the experimental setup in Fig. 2A combined with CLSM characterization. However, this technique only generates small amounts of the fibers (tens of μL/hr). Next, we discuss how the continuous production of fibers at rates of mL/hr can be realized via microfluidics and how fibers can be aligned with a custom build printer.

A microfluidic device employs a coaxial stream of toluene during fiber formation. The microfluidic setup is depicted in Fig. 8A. Two syringe pumps supply toluene and the precursor mixture via tubing into the microfluidic device. The precursor mixture enters into a dispensing needle, from which it flows into a 2–3 cm long, cylindrical, glass capillary of 50 μm inner diameter (ID). A side flushing channel allows for cleaning of the dispensing needle interior before/after use.

Toluene enters a second dispensing needle in the front of the device. From there, the toluene flows into a 2–3 cm long, cylindrical glass capillary of 300 μm ID. The 50 μm ID capillary carrying the precursor mixture stream is coaxially aligned in the 300 μm ID glass capillary. To this end, a 1–2 cm long square cross-section capillary with ID 100 μm and outer diameter 200 μm is used as an adapter (Fig. 8A). The precursor mixture enters into the coaxial flow of toluene, forms the fiber and exits the device into a toluene reservoir. This coaxial flow allows for additional control over the fiber diameter and production rate, as discussed next.

The fiber diameter and speed can be controlled with the toluene flow rate $Q_{toluene}$. Fig. 8B gives the fiber diameter and speed dependence at a constant rate of 1 mL/hr for the precursor mixture. Increasing $Q_{toluene}$ from 2.5 mL/hr to 10 mL/hr decreases the fiber diameter from 98 μm to 60 μm. Simultaneously, the fiber speed increases from 2.5 cm/s to 7.5 cm/s. The fiber thinning and speed increase result from the raise in velocity of the toluene around the fiber as depicted in Fig. 8C. In the microfluidic device, toluene drags the fiber and controls the speed [45]. The fiber speed control is important for the parallel alignment of the fibers, as discussed next. Aligning the fibers has been shown to facilitate their use as permeable transport pipes for liquid-liquid extraction [3].

Fig. 9A provides a 3D schematic depiction of a custom built printer built with LEGO® and LEGO® MINDSTORMS® parts. The microfluidic device depicted in Fig. 8A is mounted in the printer and the outlet of the largest capillary is submerged vertically in a toluene filled container. Toluene and the precursor mixture are flown into the device by means of a syringe pump. The bijel fiber flows out of the device and sinks to the bottom of the container. Simultaneously, the x- and y- motors of the printer move the device in a zig-zag pattern above the toluene filled container. If the speed of the microfluidic device movement is slower than the fiber speed (Fig. 8B), the fiber undulates during the printing.

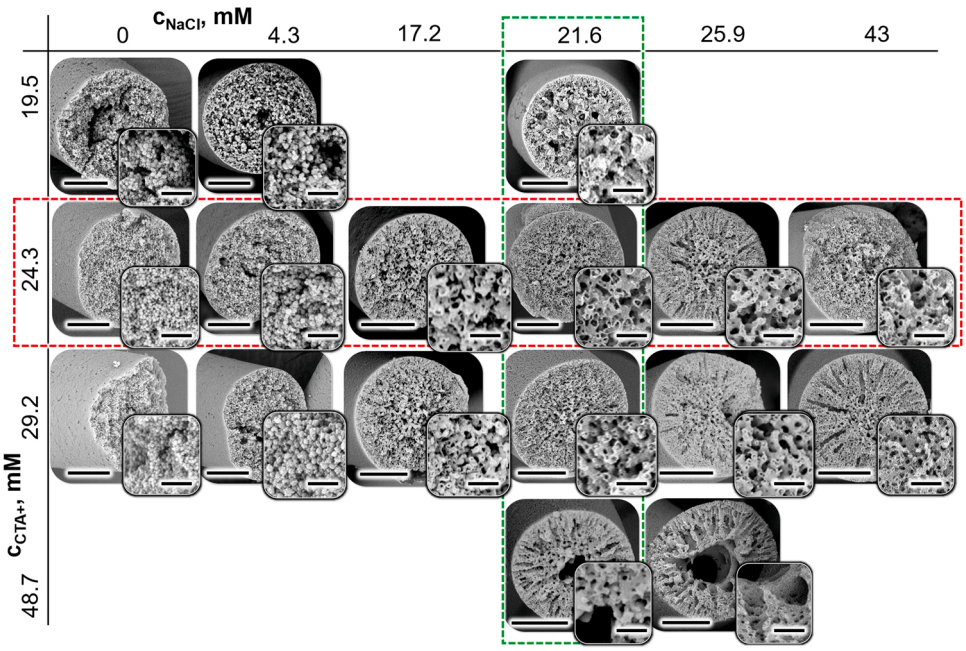

Fig. 7. Scanning electron microscopy of fibers prepared with variable c_{CTA+} and c_{NaCl}. Scale bars 25 μm, inset scale bars 5 μm.

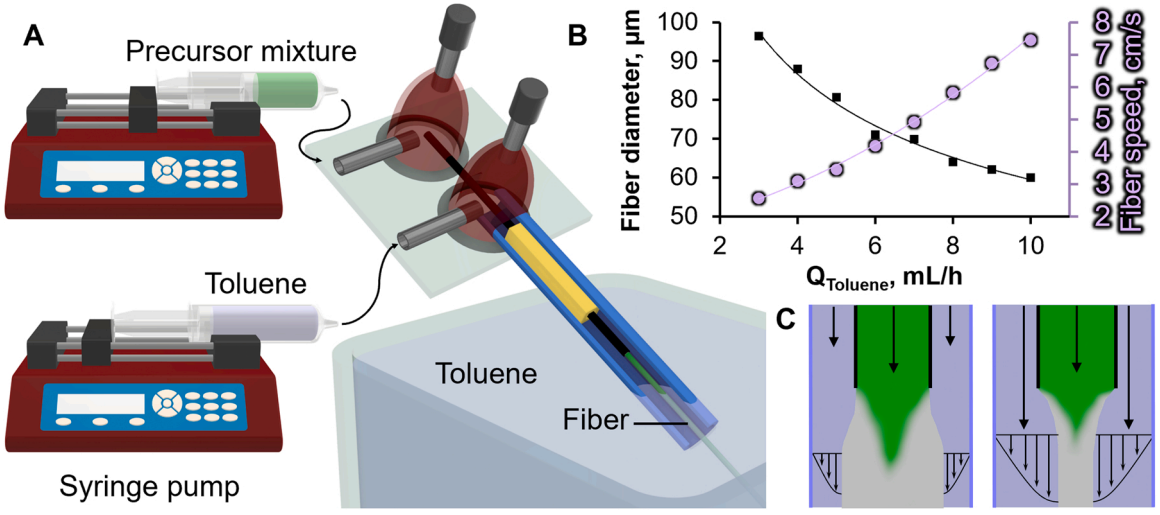

Fig. 8. Scalable fabrication of bijel fibers via STrIPS. A Schematic depiction of microfluidic setup for the continuous production of bijel fibers. The outermost capillary is shown as a cutaway drawing to reveal the internal capillaries. B Fiber diameter and speed control via the toluene flow rate. C Schematic depiction of laminar flow velocity distributions around the fibers at two different toluene flow rates.

However, when the speed of the microfluidic device movement matches or exceeds the speed of the fiber, Straight and parallel fiber segments are obtained. Fig. 9B shows a photograph and Fig. 9C a CLSM image of straight and parallel bijel fibers.

Fibers with diameters above 100 μm can be extruded with a fluidic device made with larger capillaries. The design of this device is detailed in the supporting information (SI Section 6). The resulting fibers are stored in a solution of TEOS in light mineral oil for 24 h, washed in hexane, dried and imaged with the SEM. Fig. 10 compares SEM images of fibers with diameters ranging from 90 to 300 μm. Larger diameter fibers have an increased pore size gradient over their radius. Fig. 10 shows that for a fiber with 96 μm diameter (green frame), oil channels with sizes well below 1 μm are present throughout the structure. However, as the fiber diameter is increased to 180 μm (blue frame) or 225 μm (magenta frame), the oil channel sizes in the center increase to several micrometers. The water channels are always larger in size. The graph in Fig. 10 gives the pore size of the oil and water channels in the fiber over the normalized radial coordinate (radial position R divided by outer radius R_0). Near the outer surface of the fiber ($R/R_0 \approx 1$), the smallest pores are observed. Towards the fiber center ($R/R_0 \approx 0$), the pore size grows for all fibers. The larger the fiber, the stronger the increase in pore size over R/R_0.

4. Conclusion

Based on the previously reported STrIPS method [3,21,33,46–48], this work demonstrates that bijels can be synthesized via a simplified single-channel, continuous flow process. Confocal laser scanning microscopy facilitates the visualization of nanoparticles, as well as the oil- and water- phases within the bijel, while previous reports on bijels formed via STrIPS allowed only for the visualization of the oil phase [4, 21,46,48,49]. This additional information enables the distinction

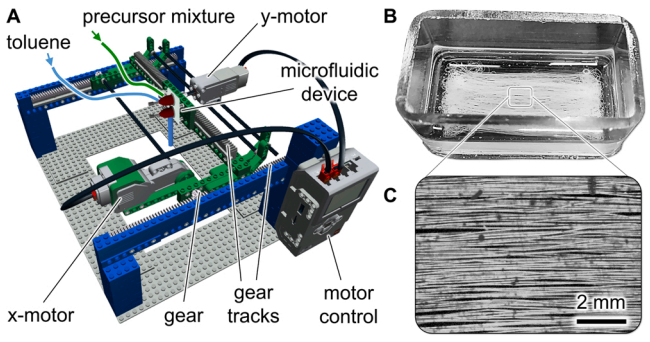

Fig. 9. Printing of bijel fibers. A 3D-schematic of the custom built Lego printer for parallel alignment of bijel fibers. B Photograph of printed fibers in toluene filled glass container. C Confocal microscopy image of parallel fibers supported on the microscope slide at the bottom of the container.

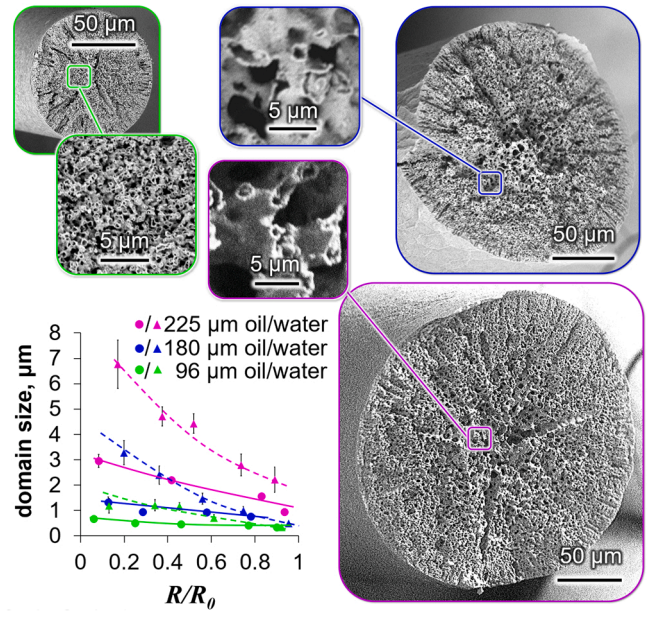

Fig. 10. SEM images of bijel fibers with variable diameters color coded in green (96 µm), blue (180 µm), magenta (225 µm) show the domain sizes of the oil (rounds) and water (triangles) channels in dependence of normalized fiber radius.

between particles at the interface and aggregates in the bulk. With this, the interfacial attachment efficiency is determined for the first time and found to reach a maximum of 19%. The present work also provides a comprehensive analysis of the colloidal and liquid phase stability of the bijel precursor mixture, while prior publications did not investigate the precursor mixture in detail [4,7,21,45,46]. It is found that stable precursor mixtures can be obtained when the CTA^+ functionalization of the silica nanoparticles is controlled via the pH value, the CTA^+ concentration (c_{CTA+}) and the aluminum content of the silica nanoparticles. Moreover, in contrast to prior reports [16,19,21,23,46,50], the control of the silica functionalization by CTA^+ facilitates the synthesis of bijels with well-defined submicrometer channels. We show how the channel uniformity can be controlled via the nanoparticle/CTA^+ interaction by variation of the pH value, c_{CTA+}, as well as the concentrations of glycerol, and NaCl [33]. Last, it is demonstrated how the production of bijel fibers with variable diameters and their parallel alignment can be achieved by combining microfluidics with a custom build printer.

The findings from this work will help researchers to synthesize bijels via STrIPS in the future. In our view, more research on STrIPS bijels is needed to transform these unique bicontinuous fluid structures into materials for energy storage, membrane separations, fuel cell components and catalytic reactors. Possible future research direction include the investigation of different liquid-liquid phase equilibria, variable viscosities of the liquids, the use of different nanoparticle materials, sizes and shapes, different surfactants, the investigation of covalent surface functionalizations of the particles, and the chemical posttreatment of the bijels for functional material fabrication.

CRediT authorship contribution statement

Alessio J. Sprockel: Conceptualization, Methodology, Investigation, Visualization. **Mohd A. Khan:** Methodology, Investigation, Visualization, Validation, Data curation, Writing – original draft. **Mariska de Ruiter:** Investigation. **Meyer T. Alting:** Investigation, Writing – original draft. **Katherine A. Macmillan:** Investigation. **Martin F. Haase:** Conceptualization, Methodology, Writing – original draft, Visualization, Supervision, Project administration, Funding acquisition.

Declaration of Competing Interest

The authors declare that they have no known competing financial interests or personal relationships that could have appeared to influence the work reported in this paper.

Data availability

Data will be made available on request.

Acknowledgments

This project has received funding from the European Research Council (ERC) under the European Union's Horizon 2020 research and innovation program (Grant agreement no. 802636). We thank Jan van Tongeren for carrying out XRF measurements and Coen Mulder for ICP-OES measurements of the Ludox TMA particles.

Appendix A. Supplementary material

Supplementary data associated with this article can be found in the online version at doi:10.1016/j.colsurfa.2023.131306.

References

[1] P.S. Clegg, Bijels: bicontinuous particle-stabilized emulsions, R. Soc. Chem. (2020).
[2] M.E. Cates, P.S. Clegg, Bijels: a new class of soft materials, Soft Matter 4 (11) (2008) 2132–2138.
[3] M.A. Khan, A.J. Sprockel, K.A. Macmillan, M.T. Alting, S.P. Kharal, S. Boakye-Ansah, M.F. Haase, Nanostructured, fluid-bicontinuous gels for continuous-flow liquid–liquid extraction, Adv. Mater. (2022), 2109547.
[4] G. Di Vitantonio, T. Wang, M.F. Haase, K.J. Stebe, D. Lee, Robust bijels for reactive separation via silica-reinforced nanoparticle layers, ACS Nano 13 (1) (2018) 26–31.
[5] S. Cha, H.G. Lim, M.F. Haase, K.J. Stebe, G.Y. Jung, D. Lee, Bicontinuous interfacially jammed emulsion gels (bijels) as media for enabling enzymatic reactive separation of a highly water insoluble substrate, Sci. Rep. 9 (1) (2019) 1–6.
[6] T. Park, G.H. Choi, D. Lee, P.J. Yoo, Metal-phenolic network-coated hollow fiber catalytic membranes via solvent transfer induced phase separation (STRIPS) for Suzuki coupling reaction, J. Membr. Sci. 634 (2021), 119386.
[7] M.F. Haase, H. Jeon, N. Hough, J.H. Kim, K.J. Stebe, D. Lee, Multifunctional nanocomposite hollow fiber membranes by solvent transfer induced phase separation, Nat. Commun. 8 (1) (2017) 1–7.
[8] H. Siegel, A.J. Sprockel, M.S. Schwenger, J.M. Steenhoff, I. Achterhuis, W.M. de Vos, M.F. Haase, Synthesis and polyelectrolyte functionalization of hollow fiber membranes formed by solvent transfer induced phase separation, ACS Appl. Mater. Interfaces, 2022.
[9] J. Witt, D. Mumm, A. Mohraz, Microstructural tunability of co-continuous bijel-derived electrodes to provide high energy and power densities, J. Mater. Chem. A 4 (3) (2016) 1000–1007.
[10] D. Cai, F.H. Richter, J.H. Thijssen, P.G. Bruce, P.S. Clegg, Direct transformation of bijels into bicontinuous composite electrolytes using a pre-mix containing lithium salt, Mater. Horiz. 5 (3) (2018) 499–505.
[11] K.M. McDevitt, D.R. Mumm, A. Mohraz, Improving cyclability of ZnO electrodes through microstructural design, ACS Appl. Energy Mater. 2 (11) (2019) 8107–8117.

[12] S.J. Gross, M.-T. Hsieh, D.R. Mumm, L. Valdevit, A. Mohraz, Alleviating expansion-induced mechanical degradation in lithium-ion battery silicon anodes via morphological design, Extrem. Mech. Lett. (2022), 101746.
[13] T.J. Thorson, E.L. Botvinick, A. Mohraz, Composite bijel-templated hydrogels for cell delivery, ACS Biomater. Sci. Eng. 4 (2) (2018) 587–594.
[14] T.J. Thorson, R.E. Gurlin, E.L. Botvinick, A. Mohraz, Bijel-templated implantable biomaterials for enhancing tissue integration and vascularization, Acta Biomater. 94 (2019) 173–182.
[15] K. Stratford, R. Adhikari, I. Pagonabarraga, J.-C. Desplat, M.E. Cates, Colloidal jamming at interfaces: a route to fluid-bicontinuous gels, Science 309 (5744) (2005) 2198–2201.
[16] E.M. Herzig, K. White, A.B. Schofield, W.C. Poon, P.S. Clegg, Bicontinuous emulsions stabilized solely by colloidal particles, Nat. Mater. 6 (12) (2007) 966–971.
[17] M.N. Lee, J.H. Thijssen, J.A. Witt, P.S. Clegg, A. Mohraz, Making a robust interfacial scaffold: Bijel rheology and its link to processability, Adv. Funct. Mater. 23 (4) (2013) 417–423.
[18] H. Ching, A. Mohraz, Bijel rheology reveals a 2D colloidal glass wrapped in 3D, Soft Matter, 2022.
[19] D. Cai, P.S. Clegg, T. Li, K.A. Rumble, J.W. Tavacoli, Bijels formed by direct mixing, Soft Matter 13 (28) (2017) 4824–4829.
[20] C. Huang, J. Forth, W. Wang, K. Hong, G.S. Smith, B.A. Helms, T.P. Russell, Bicontinuous structured liquids with sub-micrometre domains using nanoparticle surfactants, Nat. Nanotechnol. 12 (11) (2017) 1060–1063.
[21] M.F. Haase, K.J. Stebe, D. Lee, Continuous fabrication of hierarchical and asymmetric bijel microparticles, fibers, and membranes by solvent transfer-induced phase separation (STRIPS), Adv. Mater. 27 (44) (2015) 7065–7071.
[22] M. Reeves, K. Stratford, J.H. Thijssen, Quantitative morphological characterization of bicontinuous Pickering emulsions via interfacial curvatures, Soft Matter 12 (18) (2016) 4082–4092.
[23] J.W. Tavacoli, J.H. Thijssen, A.B. Schofield, P.S. Clegg, Novel, robust, and versatile bijels of nitromethane, ethanediol, and colloidal silica: capsules, sub-ten-micrometer domains, and mechanical properties, Adv. Funct. Mater. 21 (11) (2011) 2020–2027.
[24] L. Imperiali, C. Clasen, J. Fransaer, C.W. Macosko, J. Vermant, A simple route towards graphene oxide frameworks, Mater. Horiz. 1 (1) (2014) 139–145.
[25] L. Bai, J.W. Fruehwirth, X. Cheng, C.W. Macosko, Dynamics and rheology of nonpolar bijels, Soft Matter 11 (26) (2015) 5282–5293.
[26] D. Cai, P.S. Clegg, Stabilizing bijels using a mixture of fumed silica nanoparticles, Chem. Commun. 51 (95) (2015) 16984–16987.
[27] E.M. Gould, K.A. Macmillan, P.S. Clegg, Autonomous analysis to identify bijels from two-dimensional images, Soft Matter 16 (10) (2020) 2565–2573.
[28] P.S. Clegg, Characterising soft matter using machine learning, Soft Matter 17 (15) (2021) 3991–4005.
[29] K.A. White, A.B. Schofield, P. Wormald, J.W. Tavacoli, B.P. Binks, P.S. Clegg, Inversion of particle-stabilized emulsions of partially miscible liquids by mild drying of modified silica particles, J. Colloid Interface Sci. 359 (1) (2011) 126–135.
[30] B.P. Binks, S. Lumsdon, Influence of particle wettability on the type and stability of surfactant-free emulsions, Langmuir 16 (23) (2000) 8622–8631.
[31] M.F. Haase, D. Grigoriev, H. Moehwald, B. Tiersch, D.G. Shchukin, Nanoparticle modification by weak polyelectrolytes for pH-sensitive pickering emulsions, Langmuir 27 (1) (2011) 74–82.
[32] Z. Fan, L. Zhang, W. Di, K. Li, G. Li, D. Sun, Methyl-grafted silica nanoparticle stabilized water-in-oil Pickering emulsions with low-temperature stability, J. Colloid Interface Sci. 588 (2021) 501–509.
[33] S. Boakye-Ansah, M.A. Khan, M.F. Haase, Controlling surfactant adsorption on highly charged nanoparticles to stabilize bijels, J. Phys. Chem. C 124 (23) (2020) 12417–12423.
[34] P. Jiang, L. Zhang, J. Ge, G. Zhang, H. Pei, Phase inversion of emulsions stabilized by lipophilic surfactants and SiO2 nanoparticles, Colloids Surf. A Physicochem. Eng. Asp. 562 (2019) 42–53.
[35] L. Tran, M.F. Haase, Templating interfacial nanoparticle assemblies via in situ techniques, Langmuir 35 (26) (2019) 8584–8602.
[36] R. Atkin, V.S. Craig, S. Biggs, Adsorption kinetics and structural arrangements of cationic surfactants on silica surfaces, Langmuir 16 (24) (2000) 9374–9380.
[37] B.P. Binks, J.A. Rodrigues, W.J. Frith, Synergistic interaction in emulsions stabilized by a mixture of silica nanoparticles and cationic surfactant, Langmuir 23 (7) (2007) 3626–3636.
[38] M.F. Haase, J. Brujic, Tailoring of high-order multiple emulsions by the liquid–liquid phase separation of ternary mixtures, Angew. Chem. 126 (44) (2014) 11987–11991.
[39] A. Kawski, P. Bojarski, B. Kukliński, Estimation of ground-and excited-state dipole moments of Nile Red dye from solvatochromic effect on absorption and fluorescence spectra, Chem. Phys. Lett. 463 (4–6) (2008) 410–412.
[40] G.B. Alexander, R.K. Iler, Process for Modifying the Properties of A Silica Sol and Product thereof, Google Patents, 1959.
[41] T.G. Slavova, G.M. Radulova, P.A. Kralchevsky, K.D. Danov, Encapsulation of fragrances and oils by core-shell structures from silica nanoparticles, surfactant and polymer: effect of particle size, Colloids Surf. A Physicochem. Eng. Asp. 606 (2020), 125558.
[42] J. Meissner, A. Prause, B. Bharti, G.H. Findenegg, Characterization of protein adsorption onto silica nanoparticles: influence of pH and ionic strength, Colloid Polym. Sci. 293 (11) (2015) 3381–3391.
[43] R.K. Iler, The colloid chemistry of silica and silicates, LWW (1955).
[44] J.B. Segur, H.E. Oberstar, Viscosity of glycerol and its aqueous solutions, Ind. Eng. Chem. 43 (9) (1951) 2117–2120.
[45] M.F. Haase, N. Sharifi-Mood, D. Lee, K.J. Stebe, In situ mechanical testing of nanostructured bijel fibers, ACS Nano 10 (6) (2016) 6338–6344.
[46] S. Boakye-Ansah, M.S. Schwenger, M.F. Haase, Designing bijels formed by solvent transfer induced phase separation with functional nanoparticles, Soft Matter 15 (16) (2019) 3379–3388.
[47] M.F. Haase, S. Boakye-Ansah, G. Di Vitantonio, K.J. Stebe, D. Lee, Bijels formed by solvent transfer-induced phase separation, Bijels (2020) 137–166.
[48] J. Li, H. Sun, M. Wang, Phase inversion-based technique for fabricating bijels and bijels-derived structures with tunable microstructures, Langmuir 36 (48) (2020) 14644–14655.
[49] S.P. Kharal, R.P. Hesketh, M.F. Haase, High-tensile strength, composite bijels through microfluidic twisting, Adv. Funct. Mater. 30 (35) (2020), 2003555.
[50] M.A. Santiago Cordoba, J.S. Spendelow, A.N.G. Parra-Vasquez, L.A. Kuettner, P. M. Welch, C.E. Hamilton, J.A. Oertel, J.G. Duque, E.J. Meierdierks, T. A. Semelsberger, Aerobijels: ultralight carbon monoliths from cocontinuous emulsions, Adv. Funct. Mater. 30 (6) (2020), 1908383.